Fast-electron self-collimation in a plasma density gradient

Yang, X. H., Borghesi, M., & Robinson, A. P. L. (2012). Fast-electron self-collimation in a plasma density gradient. Physics of Plasmas, 19(6), -. [062702]. DOI: 10.1063/1.4729322

Published in:
Physics of Plasmas

Document Version:
Publisher's PDF, also known as Version of record

Fast-electron self-collimation in a plasma density gradient

X. H. Yang, M. Borghesi, and A. P. L. Robinson

Citation: Phys. Plasmas **19**, 062702 (2012); doi: 10.1063/1.4729322
View online: http://dx.doi.org/10.1063/1.4729322
View Table of Contents: http://pop.aip.org/resource/1/PHPAEN/v19/i6
Published by the American Institute of Physics.

Fast-electron self-collimation in a plasma density gradient

X. H. Yang,[1,2] M. Borghesi,[1] and A. P. L. Robinson[3,a)]
[1]*Centre for Plasma Physics, School of Mathematics and Physics, Queen's University of Belfast, Belfast BT7 1NN, United Kingdom*
[2]*College of Science, National University of Defense Technology, Changsha 410073, China*
[3]*Central Laser Facility, STFC Rutherford Appleton Laboratory, Chilton, Oxfordshire OX11 0QX, United Kingdom*

(Received 4 November 2011; accepted 4 May 2012; published online 15 June 2012)

A theoretical and numerical study of fast electron transport in solid and compressed fast ignition relevant targets is presented. The principal aim of the study is to assess how localized increases in the target density (e.g., by engineering of the density profile) can enhance magnetic field generation and thus pinching of the fast electron beam through reducing the rate of temperature rise. The extent to which this might benefit fast ignition is discussed. © *2012 American Institute of Physics*. [http://dx.doi.org/10.1063/1.4729322]

I. INTRODUCTION

The transport of relativistic electron beams produced during ultrahigh intense laser-plasma interaction has been studied extensively in recent years.[1–5] The most significant application of fast electrons is in the fast ignition (FI) scheme for inertial confinement fusion (ICF).[6] In this context, collimated fast electron beam transport through the overdense plasma and localized energy deposition into the core are essential requirements. This has motivated a number of theoretical and experimental studies on the collimation of fast electrons.[7–10]

A possible route to fast electron collimation is via the magnetic field generated by the resistivity of the cold target as the fast electrons propagate into the target. The amplitude of the self-generated magnetic field can reach hundreds of Tesla, which is enough to collimate the fast electrons.[11–13] However, the collimation becomes weaker for fast electron beams with large power and divergence angle, that is, resistive collimation is most effective for $I_0 < 10^{19}\,\mathrm{W/cm^2}$. Gremillet *et al.*[14] showed that the magnetic field can also induce the filamentation of fast electrons due to the magnetic repulsion of the counter propagating electron currents. Furthermore, Davies *et al.*[15,16] showed that the resistive magnetic field can change sign as the target is heated sufficiently, leading to beam hollowing rather than collimation. Several artificial approaches have been proposed to overcome this issue. Robinson and Sherlock[17] proposed to apply a material having a higher resistivity core and lower resistivity cladding to induce an azimuthal magnetic field at the interface, which has been shown to be very effective for collimating fast electrons in recent experiments.[18,19] A concept of using a generator prepulse to produce a magnetic field that collimates the fast electrons injected into the target by the main pulse has also been proposed by Robinson *et al.*[20] Recently, Sentoku *et al.*[21] demonstrated that the fast electron propagation in metals can be controlled dynamically using ionization-driven resistive magnetic field by tuning the target ionization dynamics both in experiments and numerical particle-in-cell (PIC) simulations. It is worth mentioning that fast electrons magnetic collimation in laser-compressed matter has been observed in experiment recently by Pérez *et al.*[22] Usually, numerical/analytical studies have been carried out for a solid target having a sharp vacuum-solid interface, i.e., the realistic FI scenario target is not considered. Authors such as Honrubia and Meyer-ter-Vehn[23,24] have highlighted the importance of fast electron collimation, which can enhance the energy coupling of the fast electrons with the core target and reduce the ignition energy requirements. However, to our knowledge, the effect of the resistive magnetic field has not been studied analytically for the compressed target case yet. The effect of the Coulomb collisional heating on the background is also very significant in this scenario and needs to be appropriately accounted for.[24,25]

In this paper, fast electron propagation in both solid and compressed targets is studied. The self-generated magnetic field is calculated using a rigid beam model, including both Ohmic and Coulomb collisional heating. It is found that, for compressed targets, beam hollowing is suppressed and the magnetic field increases with penetration depth of the fast electrons, suggesting that a high density background may lead to fast electron self-collimation. Fast electron propagation in targets preceded by different pedestal density and ramp profile is modeled by the 3D hybrid code ZEPHYROS,[18,19] which treats the fast electrons kinetically using the Vlasov Fokker-Planck approach and the background plasma as a resistive fluid similarly to the code of Davies *et al.*[26] The simulations show that collimated propagation of fast electrons can be enhanced in presence of an appropriate density profile.

II. THEORETICAL MODEL

As the fast electrons propagate in the target, the cold electron temperature can be obtained by the "two group" electron model from the Vlasov Fokker-Planck equation[27]

$$\frac{3}{2}n_c k\frac{\partial T_c}{\partial t} = \eta j_c^2 + \frac{3}{2}\frac{n_h k T_h}{\tau_{ch}}, \tag{1}$$

a)Electronic mail: alex.robinson@stfc.ac.uk.

where k is the Boltzmann constant, η is the resistivity of the background, j_c is the return current, $\tau_{ch} = \frac{3m_e^{1/2}(kT_h)^{3/2}}{4\sqrt{2\pi}n_c e^4 ln\Lambda}$ is the fast-cold electron collision time,[28] $ln\Lambda$ is the Coulomb logarithm, and the subscripts c and h indicate the cold and fast electrons, respectively. The thermal conduction is neglected in the above expression.

The self-generated magnetic field arising as the fast electrons propagate in the high density target is determined by the combination of the Faraday's law and Ohm's law, as

$$\frac{\partial \mathbf{B}}{\partial t} \approx \nabla \times (\eta \mathbf{j}_h). \tag{2}$$

The current density balance $j_c = -j_h$ is assumed to obtain the above equation, and the magnetic field can be expressed as two separate terms, $\eta \nabla \times \mathbf{j}_h$ and $\nabla \eta \times \mathbf{j}_h$. The first term generates a magnetic field that pinches the fast electrons, while the latter pushes the fast electrons towards the region of higher resistivity, leading to beam hollowing. To estimate the magnetic field, we will apply the "rigid beam" approach used by Davies *et al.*[15,16] In this approach, a cylindrical beam with a fixed current density that varies only with beam radius and moves with a constant velocity v along the axis is assumed. Under these conditions and in order to keep consistent with the hybrid simulations below, the fast electron current density is given by

$$j_h = -j_0 exp\left(-\left(\frac{r}{r_{spot}}\right)^8\right), \tag{3}$$

where r is the beam radius and r_{spot} is the beam spot radius. A fast electron beam with a super-Gaussian profile has usually been applied in previous studies.[24] The variables can be represented as scalars that depend only on the radius and the time

$$\tau = t - \frac{x}{v} > 0. \tag{4}$$

The resistivity is assumed to be in the form

$$\eta = \eta_0 \left(\frac{T}{T_0}\right)^{\alpha}, \tag{5}$$

where the subscript 0 indicates initial value and $\alpha = -3/2$ corresponds to the Spitzer resistivity,[29] which applies to all materials at sufficiently high temperature. In this paper, we consider, for simplicity, $\alpha = -3/2$. Substituting Eq. (5) into Eq. (1), the latter can be solved by the Euler-trapezoidal predictor-corrector method.[30]

The magnetic field can then be obtained by integrating Eq. (2) with respect to τ

$$B = \frac{d}{dr}\int j_0 \eta_0 \left(\frac{T}{T_0}\right)^{\alpha} exp\left(-\left(\frac{r}{r_{spot}}\right)^8\right) d\tau. \tag{6}$$

Substituting the temperature from Eq. (1) into the above equation, one can easily obtain the magnetic field by numerical methods.

To illustrate our discussion, we will consider a 3ω ($\lambda_0 = 0.351\,\mu$m, ω is the fundamental frequency of the Nd:glass laser, with a wavelength of 1.053 μm in vacuum) laser pulse with an intensity of $I_0 = 2 \times 10^{20}$ W/cm^2 and pulse duration of 2 ps incident on either a deuterium-tritium (DT) solid slab target with a constant density or a highly compressed DT target. Since the fast electron energy is dependent on $I_0\lambda_0^2$,[31,32] it is possible using 3ω radiation to obtain fast electrons with a range comparable to the size of the compressed target. The initial temperature and resistivity of the target are assumed to be 300 eV and $3 \times 10^{-8}\,\Omega$m. The fast electron current density can be expressed in terms of the laser intensity by $j = \alpha I/T_h$, where α is the energy fraction absorbed into electrons ($\alpha = 0.5$ (Ref. 33) is used in this paper), and T_h is the fast electron temperature given by the ponderomotive scaling.[31] Figure 1 shows the magnetic field along the beam radius given by Eq. (6) for the solid target at $t = 0.1$ ps, $t = 1$ ps, and $t = 2$ ps, respectively. The dashed lines are for the cases without collisional heating (i.e., only the first term of the left hand side of Eq. (1) is considered). It can be seen that the effect of Coulomb collisional heating on the magnetic field is initially very slight for the solid target, while it becomes more significant at later times due to the fact that a 3ω beam is applied, which could inject into the target very high densities of fast electrons (1.26×10^{28}/m^3, a factor of $\sim$3 lower than the relativistic critical density for the wavelength used here). It is also clear from the figure that the magnetic field would reverse as time increases, which then pushes the fast electrons towards the region of high resistivity, inducing beam hollowing.

The magnetic field along the beam radius for the DT compressed core slab target with a density of $n_c = 400$ g/cm^3 is shown in Fig. 2. It can be seen that the magnetic field in this case is much higher (about 5 times higher) than in the solid target. This is due to the fact that the compressed target is heated slowly by the fast electrons and the magnetic field can have enough time to grow before the resistivity decreases due to the increase of the plasma temperature. The temperature of the core target is increased significantly when the collisional heating is considered. The maximum temperature reaches 911 eV for the case with colisional heating at

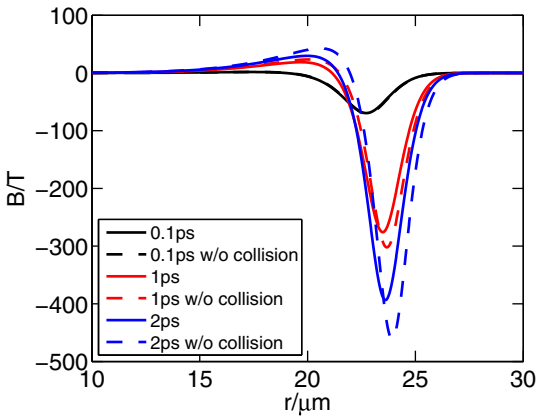

FIG. 1. The magnetic field distribution along the beam radius for the solid target ($n_c = 1$ g/cm^3) at t = 0.1 ps, t = 1 ps, and t = 2 ps, respectively. The solid lines are for the cases including collisional heating and the dashed lines are without collisional heating (same in Fig. 2).

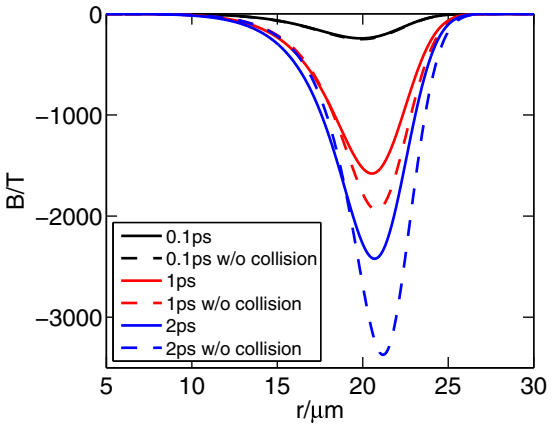

FIG. 2. The magnetic field distribution along the beam radius for the compressed core target ($n_c = 400\,\mathrm{g/cm^3}$) at t = 0.1 ps, t = 1 ps, and t = 2 ps, respectively.

$t = 2$ ps, however, it is only 705 eV for the other case. The effect of the collisional heating on the magnetic field increases significantly with time: for the time of $t = 2$ ps, the maximum magnetic field is reduced by ~950 T compared with the case without collisional heating. Moreover, the magnetic field stays negative (i.e., it does not invert its direction) and would pinch the beam (or filament it if the current profile is not homogeneous). The magnetic field increase with the background density is also shown in Fig. 3(b), in which the background plasma has a Gaussian density profile $n_c = 400\exp\left((x-100)^2/40.85^2\right)\,\mathrm{g/cm^3}$,[3,5,23] as shown in Fig. 3(a). It is shown that the magnetic field increases rapidly with the penetration depth, particularly at the edge of the beam spot radius, in agreement with Fig. 2, which shows that the maximum magnetic field appears at ~20 μm. It is interesting to note that the magnetic field at the position of the spot radius also shows a Gaussian profile along the laser axis. The fast electron beam can be collimated by the self-generated magnetic field as $R_b/R_g > \theta_{1/2}^2$,[12] where R_b is the beam radius, $R_g = \gamma m_e v_f / eB_z$ is the fast electron gyroradius,

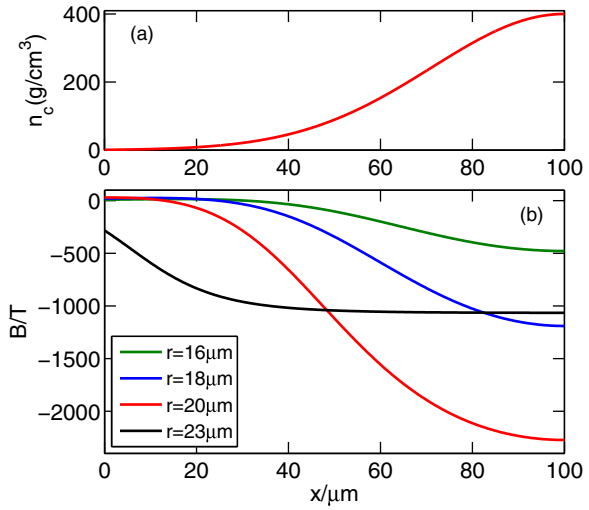

FIG. 3. The initial density profile of the target with a Gaussian density distribution ($n_c = 400\,\exp((x-100)^2/40.85^2)\,\mathrm{g/cm^3}$) (a) and magnetic field distribution (b) at different radii along the laser axis at t = 2 ps.

γ is the relativistic factor, v_f is the fast electron injection velocity, B_z is the self-generated magnetic field, and $\theta_{1/2}$ is the beam divergence angle in radians. A magnetic field of 200 T is sufficient to collimate the fast electron beam for the laser parameters considered here and fast electrons with a divergence angle of 35°.

The fact that the self-generated magnetic field increases with the penetration depth in the compressed target and does not change sign as the fast electrons propagate in the target indicates that it may be possible to collimate the fast electrons by the magnetic field in a compressed target. This analytical model assumes a constant current density throughout the whole evolution, which would lead to overestimating the magnetic field compared with a real experimental situation. We have, therefore, carried out a number of simulations using the hybrid code to examine the feasibility of this idea in more detail.

III. SIMULATION MODEL AND COMPARISON OF FAST ELECTRON PROPAGATION IN SOLID AND COMPRESSED TARGETS

In the simulations, the simulation box involves $200 \times 200 \times 200$ cells with a 1 μm transverse cell size and 0.5 μm longitudinal cell size in this section, but 1 μm longitudinal cell size in Secs. IV and V. The transverse absorption profile into fast electrons is determined by $I = \alpha I_0 \exp(-(r/r_{spot})^8)$, where $\alpha = 0.5$ is the laser absorption efficiency, $I_0 = 2 \times 10^{20}\ \mathrm{W/cm^2}$ is the laser maximum intensity, r is the radial distance from $y = z = 100\,\mu$m, and $r_{spot} = 20\,\mu$m is the laser focal spot radius. The wavelengh of the laser is set to 0.351 μm. The duration of the laser pulse is 2 ps with a top-hat profile, corresponding to an energy of 2.56 kJ absorbed into the fast electron beam. The fast electrons are injected uniformly from the left boundary ($x = 0$) with an exponential energy distribution $f(E) = \exp(-E/\langle E\rangle)/\langle E\rangle$, where $\langle E\rangle$ is the average energy of fast electrons given by the ponderomotive scaling. The half divergence angle of the fast electron is set to 35° as reported in recent PIC simulations.[34] The medium through which the electrons propagate is a DT target with an initial temperature of 300 eV.[23,24] The resistivity of the target is given by the Spitzer resistivity.[29] The specific heat capacity is determined by the same fit to the Thomas-Fermi model at constant volume used by Davies.[35] The time step is 1.25 fs (2.5 fs is used in Secs. IV and V), ~28 000 quasiparticles are injected per time step, which is 18 quasiparticles injected per time step per cell. For both the transverse and longitudinal boundaries, absorbing boundary conditions are used for the fields and particles.

The evolution of fast electron density and resistive magnetic field (B_z) for the case with a Gaussian density distribution of the background ($n_c = 400\,\exp((x-100)^2/40.85^2)\,\mathrm{g/cm^3}$) is shown in Fig. 4. It is shown that the fast electrons are collimated by the self-generated magnetic field at $x < 70\,\mu$m, but the electron beam becomes somewhat divergent for $x > 70\,\mu$m at $t = 1$ ps. However, the fast electrons can be collimated well throughout the whole propagation length at $t = 2$ ps. This is somewhat akin to the double pulse

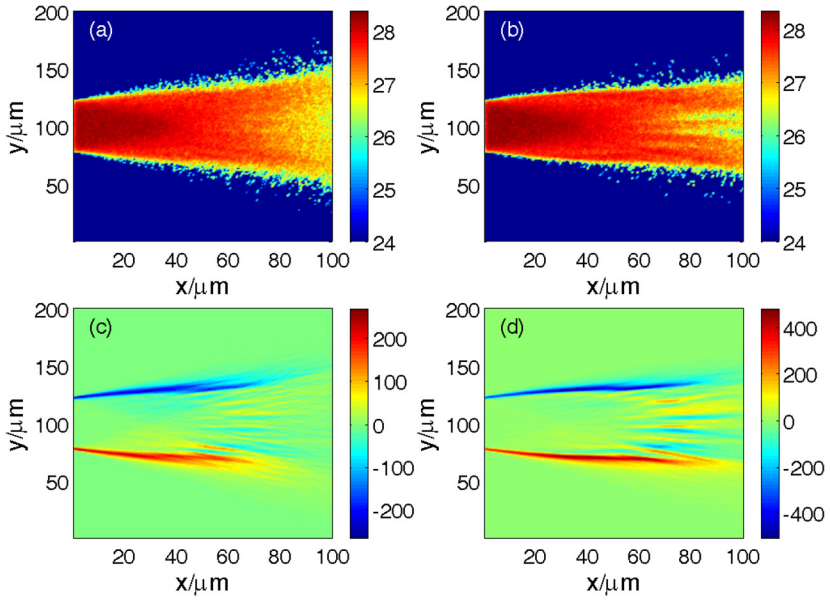

FIG. 4. log_{10} of the fast electron density [(a) and (b)] and the resistive magnetic field (B_z) [(c) and (d)] distribution for the case with a Gaussian density distribution of the cold plasma ($n_c = 400$ exp $((x-100)^2/40.85^2)$ g/cm^3) at $t = 1$ ps [(a) and (c)] and $t = 2$ ps [(b) and (d)], respectively. The density is in units of m^{-3} and the magnetic field is in units of T (same in the other figures).

approach described in Ref. 20, where the foregoing pulse generates a magnetic field that collimates the fast electrons generated by the second pulse. This indicates that a laser pulse (and the corresponding electron beam) having a long rising front could be beneficial to the fast electron collimation. It is also shown that the magnetic field around the periphery of the electron beam increases with time and extends deep into the target. However, significant increase of the magnetic field with the penetration depth as predicted by the analytical model does not occur, which can be due to the decrease of fast electron current density with the penetration depth. The magnetic field reaches 500 T at $t = 2$ ps, which is sufficient to strongly pinch the fast electrons. For comparison, Fig. 5 shows the evolution of the fast electron density and the resistive magnetic field for a solid DT target. It can be seen that the fast electron beam is divergent and propagating in the target with an open-cone profile. It is also shown that the cone angle of the fast electron beam almost remains unchanged at $t = 2$ ps compared with that of the initial stage, possibly due to the resistive magnetic field being too weak to reflect the fast electrons. Figures 5(c) and 5(d) show that the intensity of the magnetic field around the periphery of the electron beam is much weaker than in Fig. 4, and a strong magnetic field appears only near the injection surface, decreasing rapidly with the penetration depth of fast electrons. This is due to the fact that the resistivity is reduced rapidly by fast target heating by the hot electrons and that the fast electron current density decreases due to the divergent propagation.

IV. EFFECT OF PEDESTAL DENSITY ON FAST ELECTRON PROPAGATION

In the fast ignition scheme, usually a gold cone is inserted into the shell target to ensure that the fast electrons can propagate efficiently into the core. From the above

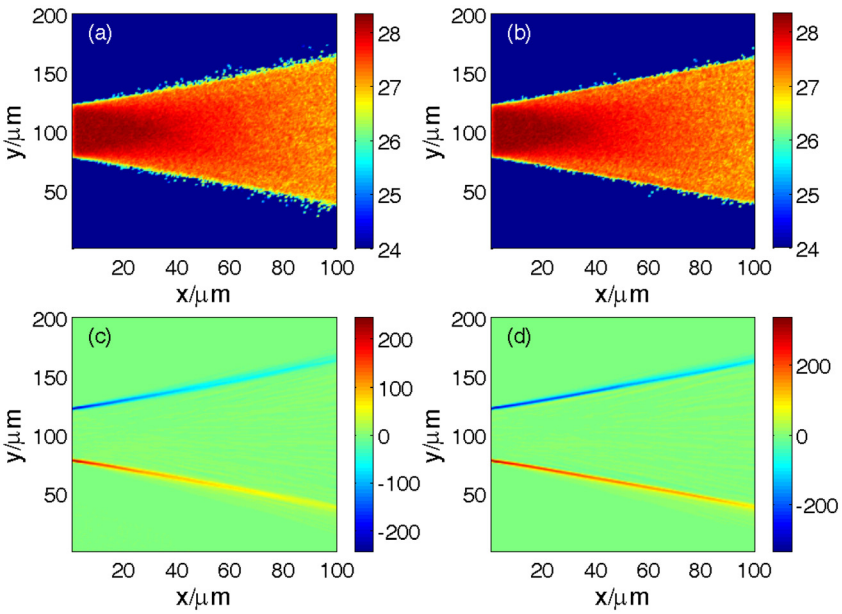

FIG. 5. log_{10} of the fast electron density [(a) and (b)] and the resistive magnetic field (B_z) [(c) and (d)] distribution for the solid DT target at $t = 1$ ps [(a) and (c)] and $t = 2$ ps [(b) and (d)], respectively.

results, we see that the fast electrons can be collimated in a density gradient, that is, the pedestal (corresponding to the position of the cone tip in the target) density could affect the fast electron propagation. We will consider the effect of the pedestal density of the target on the fast electron propagation using some more realistic target with a super-Gaussian spherical density distribution of $n_c = [n_{pedestal} + (400 - n_{pedestal})\ \exp((R-100)^4/50^4)]$ g/cm^3 as predicted by radiation-hydrodynamics simulations,[24,36] where $n_{pedestal}$ is the pedestal density, in units of g/cm^3, R is the radial distance from $x = y = z = 100\ \mu$m, in units of μm. The laser pulse is same as that used in the above studies with an intensity of 2×10^{20} W/cm^2 except that a pulse duration of 18 ps is applied here, which is consistent with the ignition energy for the target used,[36,37] corresponding to an energy of 23 kJ absorbed into the fast electron beam. Since we are mainly interested in how much energy is deposited at around a density of 350 g/cm^3, the energy coupling efficiency is defined as the fraction of the beam energy deposited in a cube centered at 350 g/cm^3 and with a side-length of 40 μm.

The fast electron density, resistive magnetic field, and the DT ion temperature are shown in Fig. 6 for the cases with a divergence of 40° and pedestal density of 5 g/cm^3 ($\rho R = 1.84$ g/cm^2) and 40 g/cm^3 ($\rho R = 1.98$ g/cm^2), respectively. It can be seen that the fast electrons are much more collimated as the pedestal density increases, which leads to a very strong magnetic field (the peak magnetic field is about 2600 T) for the case with a 40 g/cm^3 pedestal density. The maximum ion temperature reaches 5.3 KeV in both of the cases, and there are more high energy ions located in the dense core for the case with a higher pedestal density. The energy coupling efficiency is increased significantly by the collimated propagation of fast electrons, up to 18%. However, a larger fraction of energy is deposited in the pedestal for the case with a higher density pedestal (5%) compared with the other case (0.6%).

We have also performed a series of simulations with pedestal density of 5–40 g/cm^3 and divergence of 30°–50°. All the simulations show that the collimated propagation of fast electrons is enhanced with the increase of pedestal density, particularly for the cases with a smaller divergence ($\theta_{1/2} = 30°$), the fast electrons can be confined very well and propagate into the core target; a small fraction of fast electrons can pass through the core and exit the simulation box. Figure 7 shows the coupling efficiency of the injected beam as a function of the pedestal density. This shows that, in general, the dependence of coupling efficiency on pedestal density is quite weak. It can be seen that, for the smaller divergence ($\theta_{1/2} = 30°$), the coupling efficiency is increased slowly with the pedestal density as long as it stays below 30 g/cm^3 but decreases for pedestal density higher than 30 g/cm^3. This can be due to that the fast electrons losing much more energy in the pedestal as its density increases, and being slowed down before reaching the core. The energy deposited in the pedestal is 0.6% and 3.8% of the electron beam energy, respectively, for the cases with a pedestal density of 5 g/cm^3 and 40 g/cm^3. The energy coupling efficiency, for the cases with a moderate divergence ($\theta_{1/2} = 40°$), increases significantly with pedestal density because of the collimating effect of the resistive magnetic field in the higher pedestal density. Much more energy is deposited in the higher density pedestal, however, since the fast electrons

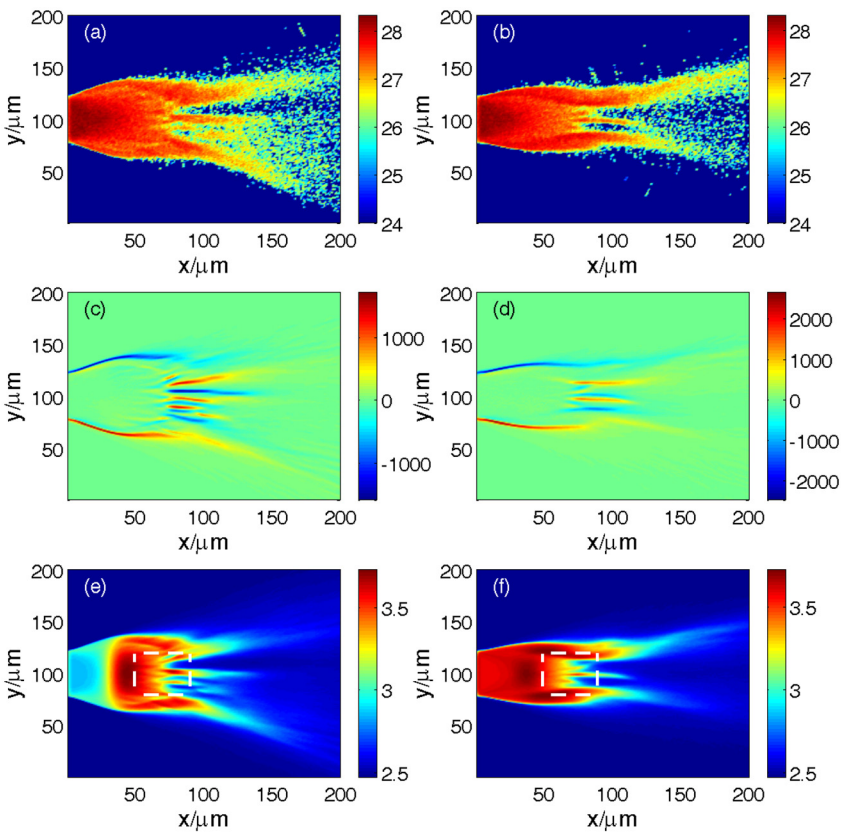

FIG. 6. log_{10} of the fast electron density [(a) and (b)], resistive magnetic field (B_z) [(c) and (d)], and log_{10} of the DT ion temperature [(e) and (f)] distribution for the compressed targets with super-Gaussian spherical density distribution of $n_c = [5 + 395\ \exp\ ((R-100)^4/50^4)]$ g/cm^3 [(a), (c), and (e)] and $n_c = [40 + 360\ \exp((R-100)^4/50^4)]$ g/cm^3 [(b), (d), and (f)], respectively. The fast electron density and magnetic field distributions are at the end of the laser pulse ($t = 18$ ps) and the ion temperature distribution is at $t = 20$ ps. The temperature is in units of eV. The dashed cube is centered at $n_c = 350$ g/cm^3 and with a side-length of 40 μm (same in Fig. 8).

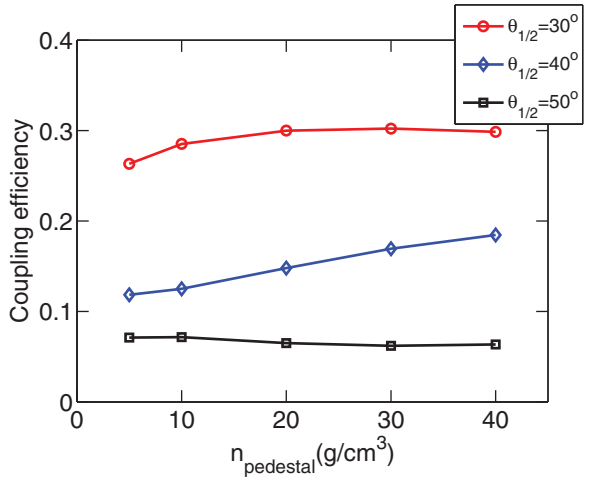

FIG. 7. Coupling efficiency of injected electron beam as a function of the pedestal density. The target density distribution is given by $n_c = [n_{pedestal} + (400 - n_{pedestal})\ \exp\ ((R-100)^4/50^4)]\ \mathrm{g/cm^3}$.

here are much more divergent, the collimating effect can lead to more fast electrons propagating into the core. The effect of pedestal density on the energy coupling efficiency is weak for the cases with a larger divergence ($\theta_{1/2} = 50°$). Though there is much more energy deposited in the whole higher density core ($n_c \geq 200\,\mathrm{g/cm^3}$) for the case with a higher pedestal density, because of the very large divergence of fast electrons, the magnetic field cannot efficiently reflect the fast electrons into the cube. That is, a higher pedestal density will only benefit the energy coupling to a significant extent provided that the fast electron beam has a moderate divergence angle. According to Atzeni's formula,[37] for the case with a pedestal density of $40\,\mathrm{g/cm^3}$ and divergence of 40°, the minimum ignition energy of 13.8 kJ should be reached for a density of $350\,\mathrm{g/cm^3}$ (corresponding to the cubic position of the target that we have chosen). The fast electron beam energy required here is at least 75 kJ to ignite the core considering a coupling efficiency of 18.46%. It should be noted that the energy coupling efficiency is less than 10% for all the cases with a divergence of 50°, that is, at least 150 kJ beam energy is required to realize the ignition. In order to reduce the ignition energy, some other collimating mechanisms, such as applying an external axial magnetic field,[38] may be required to provide sufficient collimation.

V. EFFECT OF RAMP PROFILE OF TARGET ON FAST ELECTRON PROPAGATION

To understand more thoroughly how the density gradient profile affects the fast electron propagation, we will consider the fast electrons propagating in the compressed targets with different ramp profile ($n_c = [n_{pedestal} + (400 - n_{pedestal})\ \exp((R-100)^4/R_{DT}^4)]\ \mathrm{g/cm^3}$), where R_{DT} is the core fuel radius. The divergence of fast electrons is set to 40° in this section. The laser pulse is same as that used in Sec. IV with an intensity of $2 \times 10^{20}\,\mathrm{W/cm^2}$ and a pulse duration of 18 ps, corresponding to an energy of 23 kJ absorbed into the fast electron beam. The energy coupling efficiency here is also defined as the fraction of the beam energy deposited in the cube centered at $350\,\mathrm{g/cm^3}$ and with a side-length of 40 μm.

Figure 8 shows the fast electron density, resistive magnetic field, and DT ion temperature for the cases with a pedestal density of $5\,\mathrm{g/cm^3}$ and core fuel radius of 35 μm

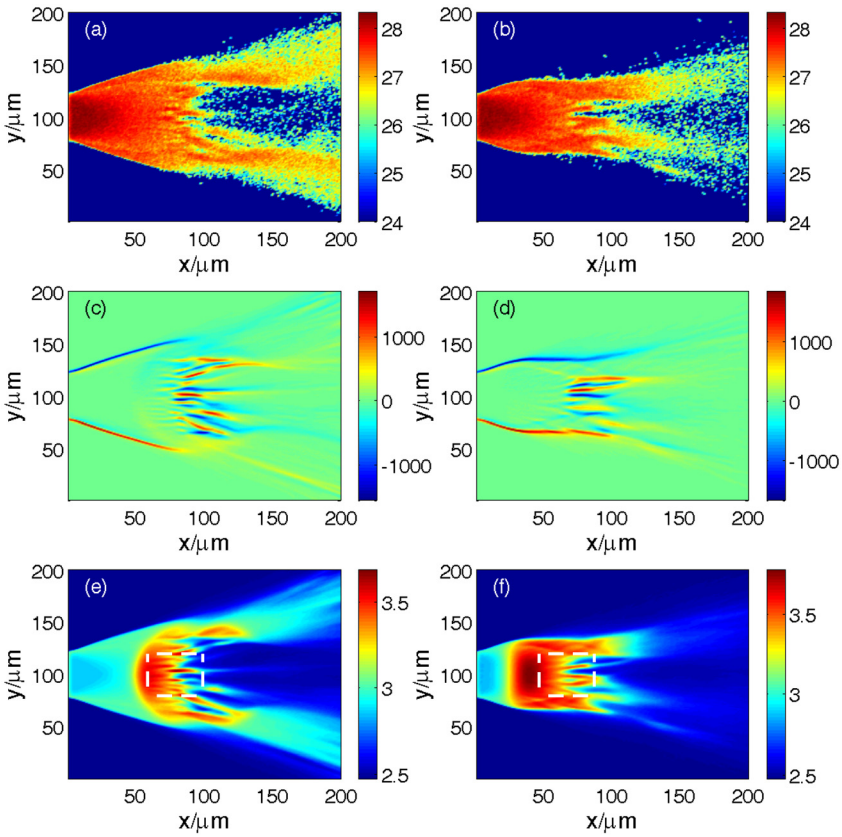

FIG. 8. log_{10} of the fast electron density [(a) and (b)], resistive magnetic field (B_z) [(c) and (d)], and log_{10} of the DT ion temperature [(e) and (f)] distribution for the compressed targets with super-Gaussian spherical density distribution of $n_c = [5 + 395\ \exp\ ((R-100)^4/35^4)]\ \mathrm{g/cm^3}$ [(a), (c), and (e)] and $n_c = [5 + 395\ \exp((R-100)^4/55^4)]\ \mathrm{g/cm^3}$ [(b), (d), and (f)], respectively.

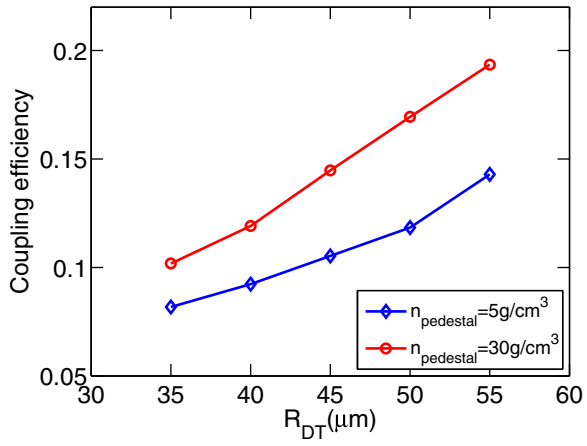

FIG. 9. Coupling efficiency of injected electron beam as a function of the core fuel radius for the cases with a initial divergence of 40°. The target density distribution is given by $n_c = [n_{pedestal} + (400 - n_{pedestal})\exp((R-100)^4/R_{DT}^4)]$ g/cm^3.

($\rho R = 1.3$ g/cm^2) and 55 μm ($\rho R = 2.02$ g/cm^2), respectively. It can be seen that the fast electron beam radius is reduced significantly for the case with a larger spot radius. This is due to the higher target areal density seen by fast electrons along the propagation path for the case with a larger spot radius, which can generate much stronger magnetic field to confine the beams, as shown in Figs. 8(c) and 8(d). It is shown that the ion temperature in the cube is much higher for the case with larger spot radius compared with the other case, because a larger fraction of fast electrons escape via the end wall in the latter case. The energy lost via the end wall reaches 48.13% for the case with a 35 μm spot radius due to the smaller areal density and divergent fast electron propagation, significantly higher than in the other case (only 7.57%), leading to a significant decrease of energy coupling efficiency (8.18%) compared with the latter (14.29%).

We have carried out simulations using targets with different spot radius and pedestal density in order to find the dependence of the fast electron propagation on the ramp profile of target in detail. It is found that, for a given pedestal density, the maximum beam radius decreases with increase of core fuel radius, suggesting that a density gradient with a gradual ramp profile can enhance the fast electron collimation. The dependence of fast electron coupling efficiency on the core fuel radius is shown in Fig. 9. It can be seen that the energy coupling efficiency increases as R_{DT} increases. This is because the effect of magnetic collimation gets stronger as R_{DT} increases, as was previously illustrated by Fig. 8. It is also shown that the higher pedestal density can increase the energy coupling efficiency for the target considered here. It is indicated that, for a given maximum core density, a target with a slowly increasing density profile (i.e., larger R_{DT}) could be beneficial to the fast electron collimated propagation and energy coupling.

VI. CONCLUSION

In summary, this paper has studied the effect that plasma density has on fast electron propagation in solid and compressed DT targets of relevance to fast ignition ICF. It was conjectured that increasing the density would increase the specific heat capacity, slow the rate of temperature increase, and thus enhance magnetic field generation. It was further thought that this might have a beneficial effect in fast ignition. In simple scenarios, this effect was verified and observed clearly (Sec. III).

In fast ignition relevant targets, this was studied in terms of both the "pedestal" density and the "core profile." The effects of changing the "pedestal" density are quite weak overall, although some benefit might be obtained from a high density pedestal (40 g/cm^3). The radial extent of the compressed core (assuming a fixed maximum density) can have a strong effect on the coupling efficiency, but this implies a change to the ρR of the compressed fuel which may be difficult to achieve.

Any benefits that may be obtained from manipulating the density profile can only be obtained provided that the cone tip is not destroyed by the fuel assembly. The effects on the cone tip have not been studied here and will have to be examined closely in future studies.

ACKNOWLEDGMENTS

This work was supported by EPSRC (Grant No. EP/D06337X/1) and partly supported in the framework of the HiPER consortium. X.H.Y. also acknowledges the support from the China Scholarship Council, the NSFC (Grant Nos. 10975185 and 10976031), the Innovation Foundation for Postgraduate of Hunan Province (Grant No. CX2010B008) and NUDT (Grant No. B100204). The authors are grateful for computational resources provided by STFC's e-Science facility.

[1]M. Borghesi, A. J. Mackinnon, A. R. Bell, G. Malka, C. Vickers, O. Willi, J. R. Davies, A. Pukhov, and J. Meyer-ter-Vehn, Phys. Rev. Lett. **83**, 4309 (1999).
[2]A. R. Bell, J. R. Davies, S. Guerin, and H. Ruhl, Plasma Phys. Controlled Fusion **39**, 653 (1997).
[3]R. J. Mason, Phys. Rev. Lett. **96**, 035001 (2006).
[4]J. J. Santos, A. Debayle, Ph. Nicolaï, V. Tikhonchuk, M. Manclossi, D. Batani, A. Guemnie-Tafo, J. Faure, V. Malka, and J. J. Honrubia, Phys. Plasmas **14**, 103107 (2007).
[5]A. A. Solodov, K. S. Anderson, R. Betti, V. Gotcheva, J. Myatt, J. A. Delettrez, S. Skupsky, W. Theobald, and C. Stoeckl, Phys. Plasmas **16**, 056309 (2009).
[6]M. Tabak, J. Hammer, M. E. Glinsky, W. L. Kruer, S. C. Wilks, J. Woodworth, E. M. Campbell, M. D. Perry, and R. J. Mason, Phys. Plasmas **1**, 1626 (1994).
[7]R. B. Campbell, J. S. DeGroot, T. A. Mehlhorn, D. R. Welch, and B. V. Oliver, Phys. Plasmas **10**, 4169 (2003).
[8]R. Kodama, Y. Sentoku, Z. L. Chen, G. R. Kumar, S. P. Hatchett, Y. Toyama, T. E. Cowan, R. R. Freeman, J. Fuchs, Y. Izawa, M. H. Key, Y. Kitagawa, K. Kondo, T. Matsuoka, H. Nakamura, M. Nakatsutsumi, P. A. Norreys, T. Norimatsu, R. A. Snavely, R. B. Stephens, M. Tampo, K. A. Tanaka, and T. Yabuuchi, Nature (London) **432**, 1005 (2004).
[9]X. H. Yang, H. Xu, Y. Y. Ma, F. Q. Shao, Y. Yin, H. B. Zhuo, M. Y. Yu, and C. L. Tian, Phys. Plasmas **18**, 023109 (2011).
[10]H. B. Cai, S. P. Zhu, M. Chen, S. Z. Wu, X. T. He, and K. Mima, Phys. Rev. E **83**, 036408 (2011).
[11]J. R. Davies, A. R. Bell, and M. Tatarakis, Phys. Rev. E **59**, 6032 (1999).
[12]A. R. Bell and R. J. Kingham, Phys. Rev. Lett. **91**, 035003 (2003).
[13]M. Storm, A. A. Solodov, J. F. Myatt, D. D. Meyerhofer, C. Stoeckl, C. Mileham, R. Betti, P. M. Nilson, T. C. Sangster, W. Theobald, and C. Guo, Phys. Rev. Lett. **102**, 235004 (2009).
[14]L. Gremillet, G. Bonnaud, and F. Amiranoff, Phys. Plasmas **9**, 941 (2002).
[15]J. R. Davies, Phys. Rev. E **68**, 056404 (2003).

[16]J. R. Davies, J. S. Green, and P. A. Norreys, Plasma Phys. Controlled Fusion **48**, 1181 (2006).
[17]A. P. L. Robinson and M. Sherlock, Phys. Plasmas **14**, 083105 (2007).
[18]S. Kar, A. P. L. Robinson, D. C. Carroll, O. Lundh, K. Markey, P. McKenna, P. Norreys, and M. Zepf, Phys. Rev. Lett. **102**, 055001 (2009).
[19]B. Ramakrishna, S. Kar, A. P. L. Robinson, D. J. Adams, K. Markey, M. N. Quinn, X. H. Yuan, P. McKenna, K. L. Lancaster, J. S. Green, R. H. H. Scott, P. A. Norreys, J. Schreiber, and M. Zepf, Phys. Rev. Lett. **105**, 135001 (2010).
[20]A. P. L. Robinson, M. Sherlock, and P. A. Norreys, Phys. Rev. Lett. **100**, 025002 (2008).
[21]Y. Sentoku, E. d'Humières, L. Romagnani, P. Audebert, and J. Fuchs, Phys. Rev. Lett. **107**, 135005 (2011).
[22]F. Pérez, A. Debayle, J. Honrubia, M. Koenig, D. Batani, S. D. Baton, F. N. Beg, C. Benedetti, E. Brambrink, S. Chawla, F. Dorchies, C. Fourment, M. Galimberti, L. A. Gizzi, L. Gremillet, R. Heathcote, D. P. Higginson, S. Hulin, R. Jafer, P. Koester, L. Labate, K. L. Lancaster, A. J. MacKinnon, A. G. MacPhee, W. Nazarov, P. Nicolai, J. Pasley, R. Ramis, M. Richetta, J. J. Santos, A. Sgattoni, C. Spindloe, B. Vauzour, T. Vinci, and L. Volpe, Phys. Rev. Lett. **107**, 065004 (2011).
[23]J. J. Honrubia and J. Meyer-ter-Vehn, Nucl. Fusion **46**, L25 (2006).
[24]J. J. Honrubia and J. Meyer-ter-Vehn, Plasma Phys. Controlled Fusion **51**, 014008 (2009).
[25]A. J. Kemp, Y. Sentoku, V. Sotnikov, and S. C. Wilks, Phys. Rev. Lett. **97**, 235001 (2006).
[26]J. R. Davies, A. R. Bell, M. G. Haines, and S. M. Guérin, Phys. Rev. E **56**, 7193 (1997).
[27]M. E. Glinsky, Phys. Plasmas **2**, 2796 (1994).
[28]J. D. Huba, *NRL Plasma Formulary* (Naval Research Laboratory, Washington, DC, 2009).
[29]L. Spitzer and R. Härm, Phys. Rev. **89**, 977 (1953).
[30]W. F. Ames, *Numerical Methods for Partial Differential Equations* (Academic, New York, 1977), pp. 85–89.
[31]S. C. Wilks, W. L. Kruer, M. Tabak, and A. B. Langdon, Phys. Rev. Lett. **69**, 1383 (1992).
[32]F. N. Beg, A. R. Bell, A. E. Dangor, C. N. Danson, A. P. Fews, M. E. Glinsky, B. A. Hammel, P. Lee, P. A. Norreys, and M. Tatarakis, Phys. Plasmas **4**, 447 (1997).
[33]M. Tabak, D. S. Clark, S. P. Hatchett, M. H. Key, B. F. Lasinski, R. A. Snavely, S. C. Wilks, R. P. J. Town, R. Stephens, E. M. Campbell, R. Kodama, K. Mima, K. A. Tanaka, S. Atzeni, and R. Freeman, Phys. Plasmas **12**, 057305 (2005).
[34]J. C. Adam, A. Héron, and G. Laval, Phys. Rev. Lett. **97**, 205006 (2006).
[35]J. R. Davies, Phys. Rev. E **65**, 026407 (2002).
[36]S. Atzeni, A. Schiavi, J. J. Honrubia, X. Ribeyre, G. Schurtz, Ph. Nicolaï, M. Olazabal-Loumé, C. Bellei, R. G. Evans, and J. R. Davies, Phys. Plasmas **15**, 056311 (2008).
[37]S. Atzeni, Phys. Plasmas **6**, 3316 (1999).
[38]X. H. Yang, M. Borghesi, B. Qiao, M. Geissler, and A. P. L. Robinson, Phys. Plasmas **18**, 093102 (2011).